Supporting Information for:

Identification of defects in pure and Al/Ga-doped ZnO to improve X-ray detector performance: Experimental and Simulation

Mohammad Rostami[1,*], Mehdi Janbazi[2,**], Ali Biganeh[2], Farnaz Ghavami[1]

[1] Faculty of Physics, Kharazmi University, Tehran, Iran
[2] Physics and Accelerators School, Nuclear Sciences and Technology Research Institute, Tehran, Iran
* Corresponding author, Email address: mrostami@khu.ac.ir
**Corresponding author, Email address: mehdijanbazi@yahoo.com

S1. Rationale for the Selection of Calcination Temperatures and Doping Levels

We selected a calcination temperature range of 400–600 °C because both theoretical and experimental studies indicate that this is the equilibrium region for ZnO [1]. Besides, according to DFT defect formation energy calculations, the number of intrinsic defects is minimized in this temperature range, which is essential for X-ray detectors where fewer traps and lower carrier concentrations are preferred. Additionally, EDX analyses reveal that dopant incorporation is highly temperature-dependent. At 500 °C, Al and Ga are incorporated more efficiently and with fewer defects compared to 600 °C. Therefore, we selected temperatures of 400, 500, and 600 °C to cover the equilibrium range and examine how both defect density and dopant incorporation affect the material properties. Furthermore, both experimental observations and computational feasibility guided the selection of 3% and 5% doping concentrations. At low doping levels (1%), only slight changes in trap density and photoluminescence were detected, while accurate simulations at this concentration would require prohibitively large supercells. On the other hand, higher concentrations (7–9%) were found to distort the ZnO crystal structure and introduce excessive defects, which are detrimental to detector performance. Therefore, we chose doping levels of 3% and 5%, as they balance maintaining the ZnO crystal structure with producing noticeable changes in electronic and optical properties, while avoiding excessive defect formation.

S2. Theoretical Background

S2.1. EPR theory:

The dynamics of the spin of an electron (S) in a material that has a nucleus with spin I, in a magnetic field (B), are explained by the spin Hamiltonian, which is represented [2]:

$$\hat{H}_s = \mu_B \hat{S} g B + \hat{S} A \hat{I} \qquad (S1),$$

The g-tensor is defined in the following way:

$$g_{ij} = g_e \delta_{ij} + \Delta g^{RM}_{ij} + \Delta g^{CG}_{ij} + \Delta g^{OZ/SOC}_{ij} \qquad (S2),$$

where g_e is the value of the g factor associated with a free electron (2.0023193), and the relativistic mass and gauge corrections are represented by Δg^{RM} and Δg^{CG}, respectively. These corrections generally have a minimal effect and can often be overlooked without much consequence. The term $\Delta g^{oz/soc}$ considers the relationship of orbital Zeeman (OZ) and spin-orbit coupling (SOC) [2]:

$$\Delta g_{\mu\nu}^{OZ/SOC} = \frac{g_e \mu_\beta^3}{2\pi\varepsilon_0 hc^2} \frac{1}{\langle S_z \rangle} \times \sum_X Z_X \sum_X \left\{ \frac{\left\langle \Psi_0^{(0)} \middle| \sum_i \frac{1}{r_{iX}^3} \times (I_{iX})_\mu S_{jz} \middle| \Psi_n^{(0)} \right\rangle \left\langle \Psi_0^{(0)} \middle| \sum_j (I_{iX})_\nu \middle| \Psi_n^{(0)} \right\rangle}{E_0^{(0)} - E_n^{(0)}} \right\} \quad (S3).$$

Here, i and j denote the electron index, and X denotes the nucleus index (e.g., the X-th nucleus). The unperturbed wave functions $\psi_0^{(0)}$ and $\psi_n^{(0)}$ are associated with the ground state and the nth excited state, with the energy levels $E_0^{(0)}$ and $E_n^{(0)}$, respectively. The term $\hat{S}A\hat{I}$ mentioned in Eq. (1) defines the hyperfine interaction using the hyperfine coupling tensor (A). The A tensor could be broken down into two parts:

$$A(X) = A^{iso}(X) I_3 + A^{dip}(X) \quad (S4),$$

where $A^{iso}(X)$ refers to the isotropic Fermi contact interaction, while $A^{dip}(X)$ indicates the dipolar part of the HFCC. The isotropic Fermi contact interaction, $A^{iso}(X)$, is associated with the spin density (ρ_X) found at a specific nucleus and is described by [3]:

$$A_X^{iso} = \frac{4\pi}{3} \mu_\beta \mu_X g_e g_X \frac{1}{\langle S_Z \rangle} \rho_X^{\alpha-\beta} \quad (S5),$$

The spin density, denoted as $\rho_X^{\alpha-\beta}$, is calculated based on the difference in density matrices between states α and β for nucleus X.

S2.2. Electron and hole concentration:

The band structure diagrams provide essential information for the physical, transport, and optical properties. In quantum mechanics, a carrier (electron or hole) is considered a wave packet, and its energy is represented in this way:

$$E = \frac{\hbar^2 k^2}{2m^*} \quad (S6),$$

where m^* and k represent the carrier's effective mass and wavenumber, respectively. The effective masses of electrons (m_e^*) and holes (m_h^*) can be obtained from the band structure as follows:

$$m^* = \hbar^2 \left(\frac{\partial^2 E}{\partial k^2}\right)^{-1} \qquad (S7).$$

The effective density of states in the valence (N_v) and conduction (N_c) bands at the temperature T is found by [4–7]:

$$N_v = 2\left(\frac{2\pi k_B T m_h^*}{h^2}\right)^{\frac{3}{2}} \qquad (S8)$$

$$N_c = 2\left(\frac{2\pi k_B T m_e^*}{h^2}\right)^{\frac{3}{2}} \qquad (S9)$$

where k_B is the Boltzmann constant. he carrier concentration is also calculated as follows [4–6]:

$$n = N_C \exp\left(-\frac{(E_c - E_F)}{k_B T}\right) \qquad (S10)$$

$$p = N_v \exp\left(-\frac{(E_F - E_v)}{k_B T}\right) \qquad (S11)$$

where E_F, E_c, and E_v are the are the Fermi energy, the conduction band minimum, and the valence band maximum, respectively.

S3. Comparison with previous studies on ZnO defects

Previous computational investigations have mainly examined formation energies and band structures of ZnO defects. In contrast, our work employs computational EPR analysis to establish a meaningful connection between the spin-resolved electronic structure and the observed optical transitions, thereby providing a more comprehensive understanding of how specific defect complexes influence photoluminescence behavior. In this paper, we examined individual defects in ZnO as well as the defect complexes with defects at varying separations. Although previous studies have considered simultaneous defect configurations, our work provides a more detailed analysis using computational EPR spectroscopy. Among the defects, zinc vacancies are of particular interest, as they enhance photoluminescence and are mainly responsible for the characteristic blue emission (2.48–2.75) often observed in doped ZnO [8]. Oxygen vacancies are known to introduce energy levels in the band gap, which can lead to visible light emissions—typically in the green and blue regions [9]. We have also observed the same emission in the band structures of the Al- and Ga-doped samples containing Zn and O vacancies (see Figs. S10 to S13).

R. Vidya et al. have demonstrated that, based on the energy states of intrinsic defects and their complexes in ZnO, derived from a density functional theory pseudopotential all-electron approach, green luminescence (GL) is proposed to originate from a V_{Zn}–V_O defect complex [10–12]. Similarly, our findings also identify $ZnOV_{OZn}^{'}$ as the source of the transition that leads to a green light, as illustrated in Fig. 8. Moreover, in this study, we have confirmed the existence of such defect complexes through computational EPR spectroscopy, a method rarely employed in this context. Additionally, our computational EPR analysis suggests that impurity substitution at oxygen sites (Al_O defect) is negligible (see Fig. 7), with dopant atoms preferentially occupying zinc sites, consistent with previous findings obtained through other methods [13].

From an electrical point of view, zinc interstitials behave as shallow donors, releasing electrons into the conduction band, which results in n-type conductivity. In contrast, oxygen interstitials create deeper states that may lower optical transparency and slightly alter the material's surface reactivity. In the band structure diagrams of the 3% doped samples containing the V_{OZn} complex defects, transition emissions related to deep traps in the red region (1.65–2.00 eV) were identified (see Figs. S10 and S12), a phenomenon that previous works on defect complexes have reported [14,15]. Regarding the formation energy, we found that V_O is among the most stable defects in pure ZnO, with the formation energy of V_{Zn} being slightly lower than that of V_O, making V_O the most stable defect. L. Cabral et al. reported that V_O is one of the most stable defects, in agreement with the general trend observed among the intrinsic defects [16]."

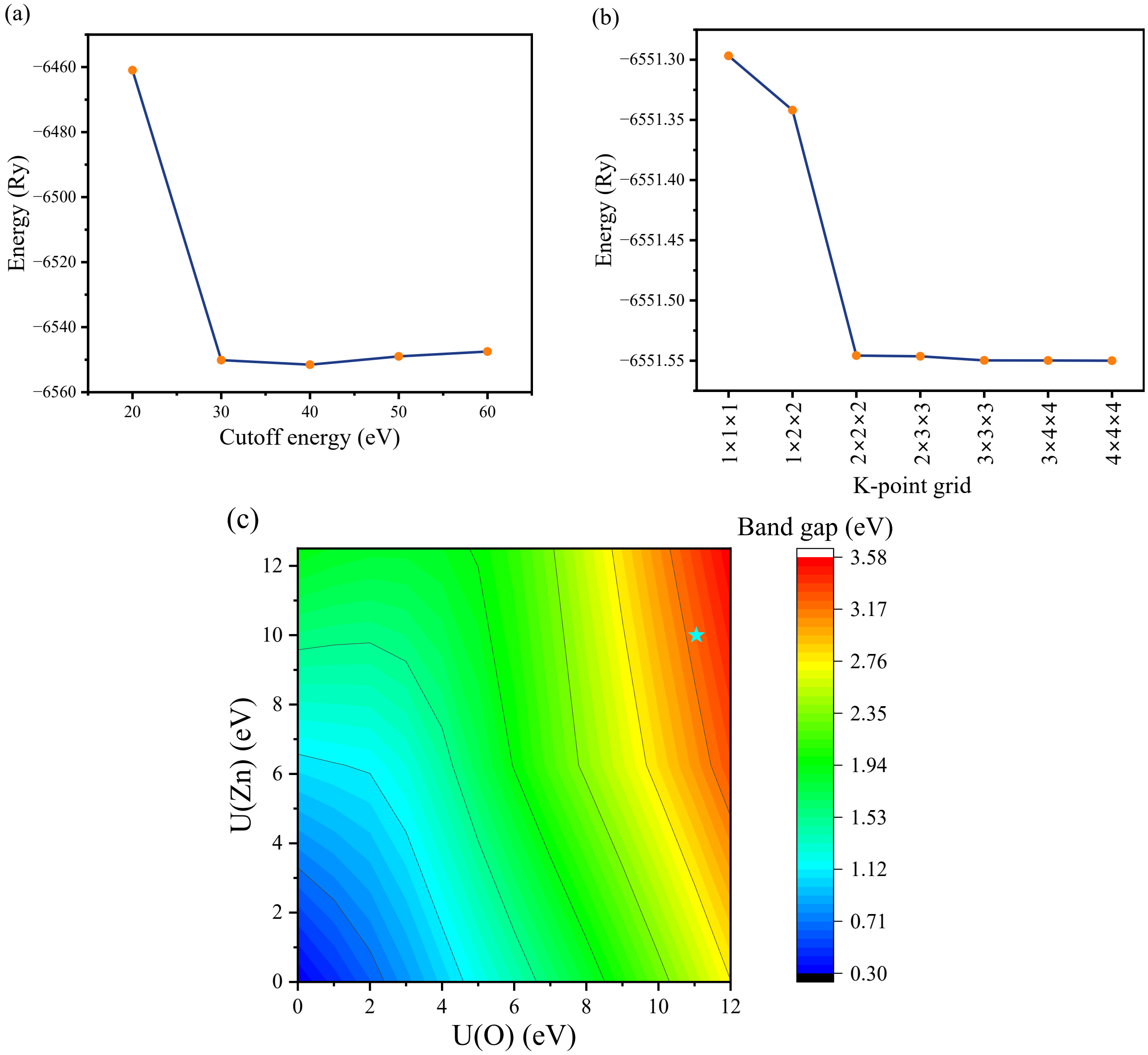

Fig. S1. Convergence tests for the DFT+U framework: (a) plane-wave cutoff energy, (b) k-point grid sampling, and (c) Hubbard U parameters. The optimum U parameters, determined by band gap alignment, are marked by a star in (c).

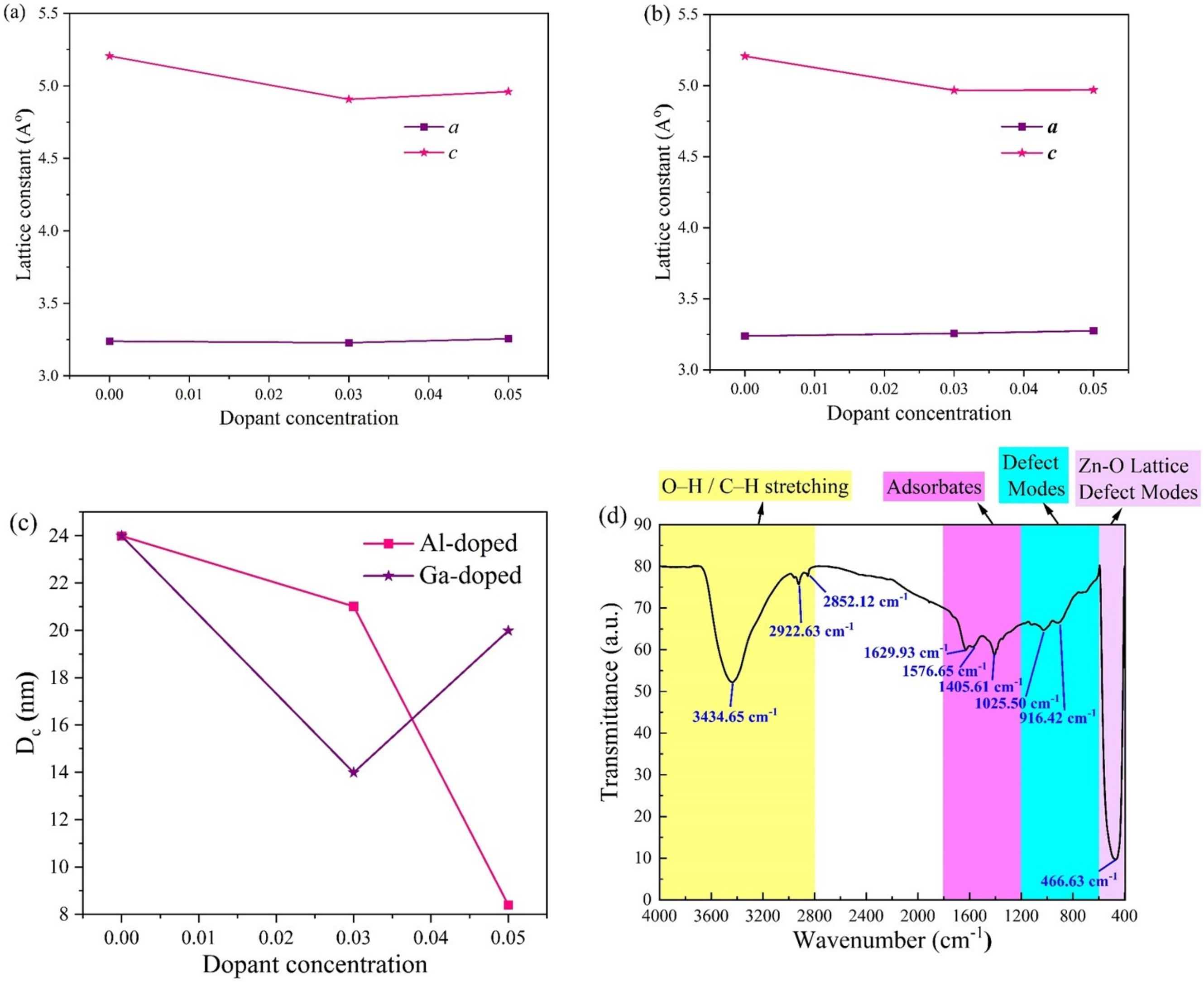

Fig. S2. The hexagonal lattice parameters for (a) Al-doped, and (b) Ga-doped samples, (c) the crystallite size of the pure and doped nanoparticles, and (d) the FTIR spectra of the pure sample calcinated at 400°C.

.

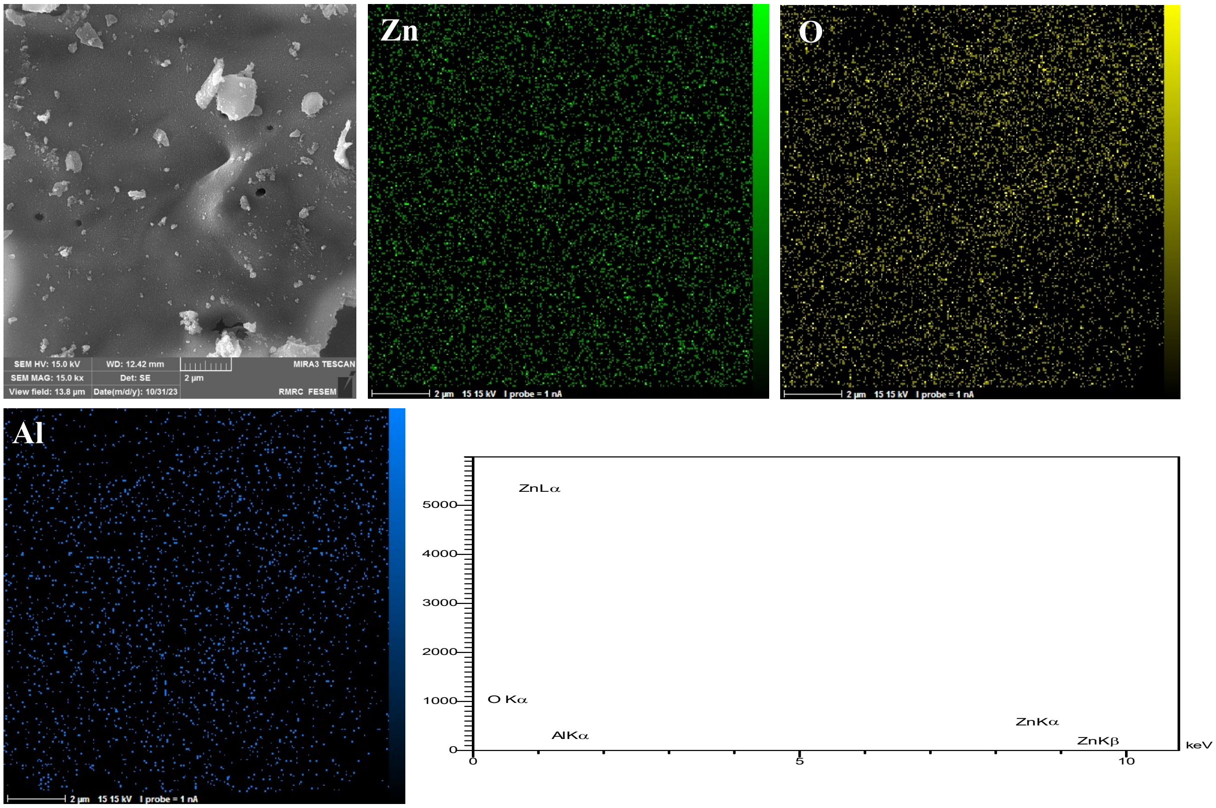

Fig. S3. EDS elemental maps (Zn, O, and Al) obtained from ZnO:Al (3%) sample.

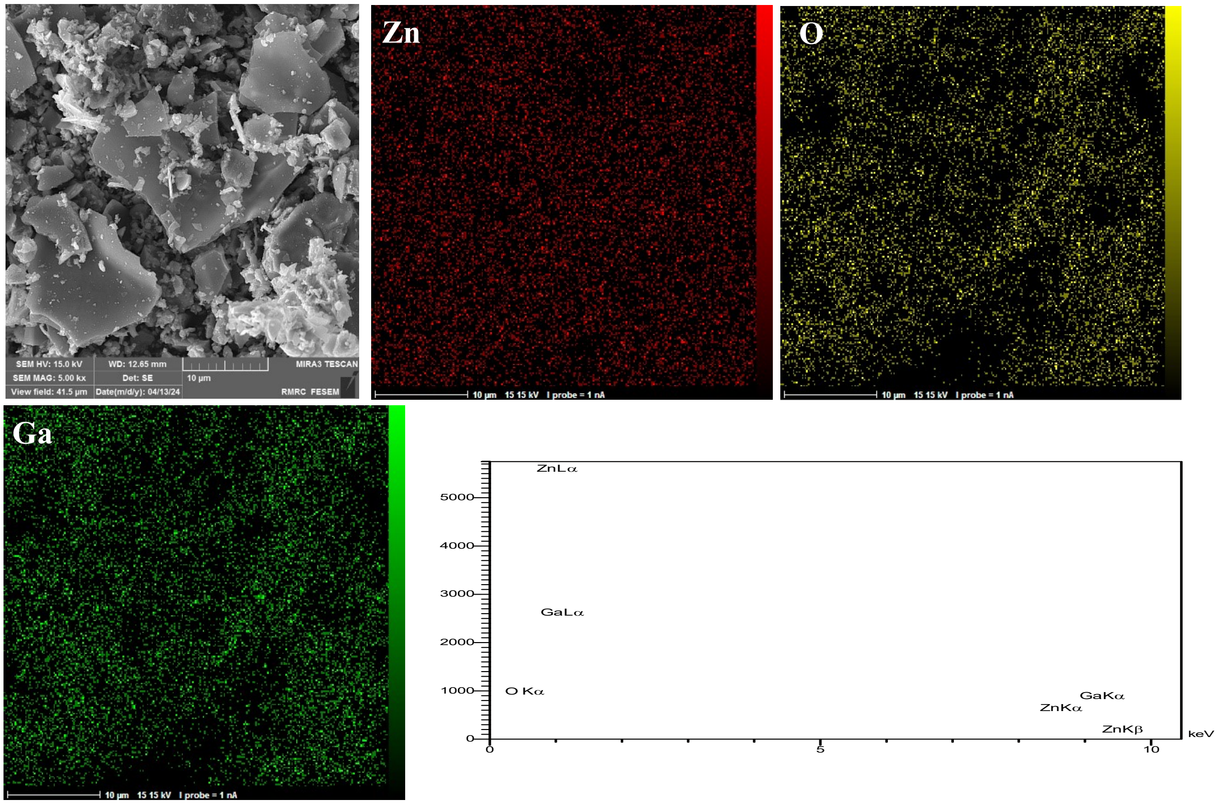

Fig. S4. EDS elemental maps (Zn, O, and Ga) obtained from ZnO:Ga (3%) sample.

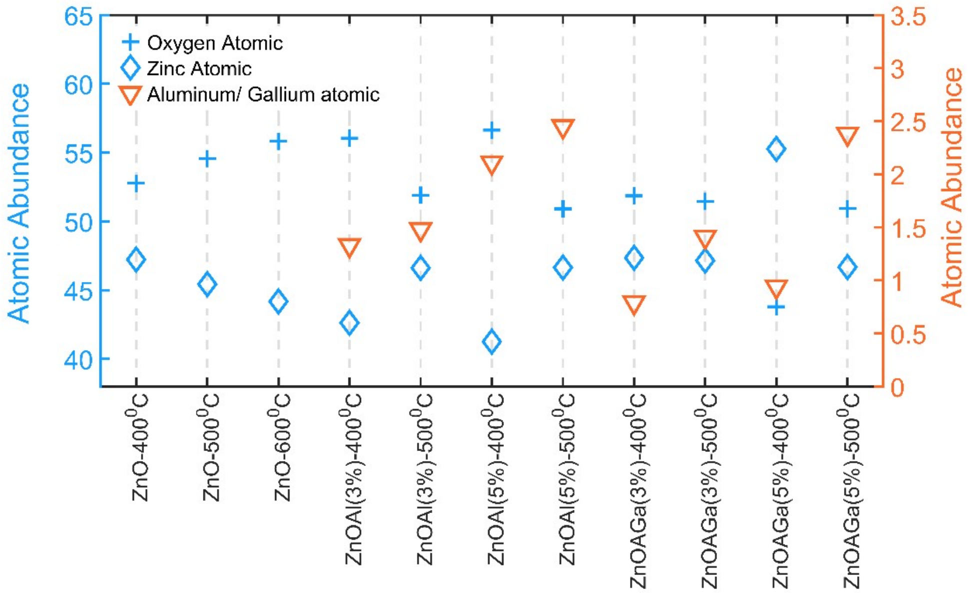

Fig. S5. The abundance percentages of oxygen, zinc, aluminum, and gallium atoms obtained using EDS analysis.

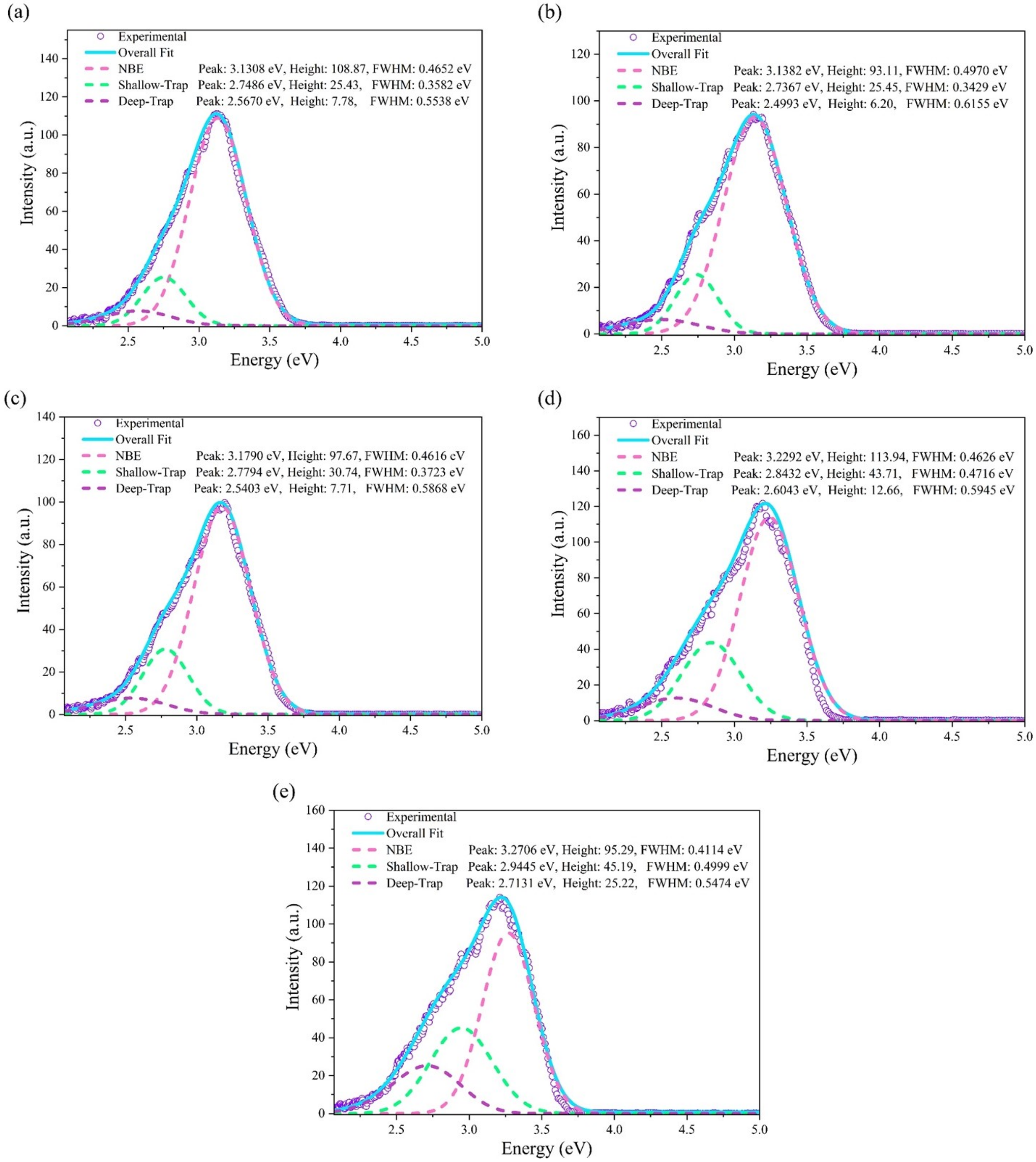

Fig. S6. The deconvolution of the PL spectra for (a) pure, (b) Al-3, (c) Ga-3, (d) Al-5, and (e) Ga-5 samples calcinated at 400°C.

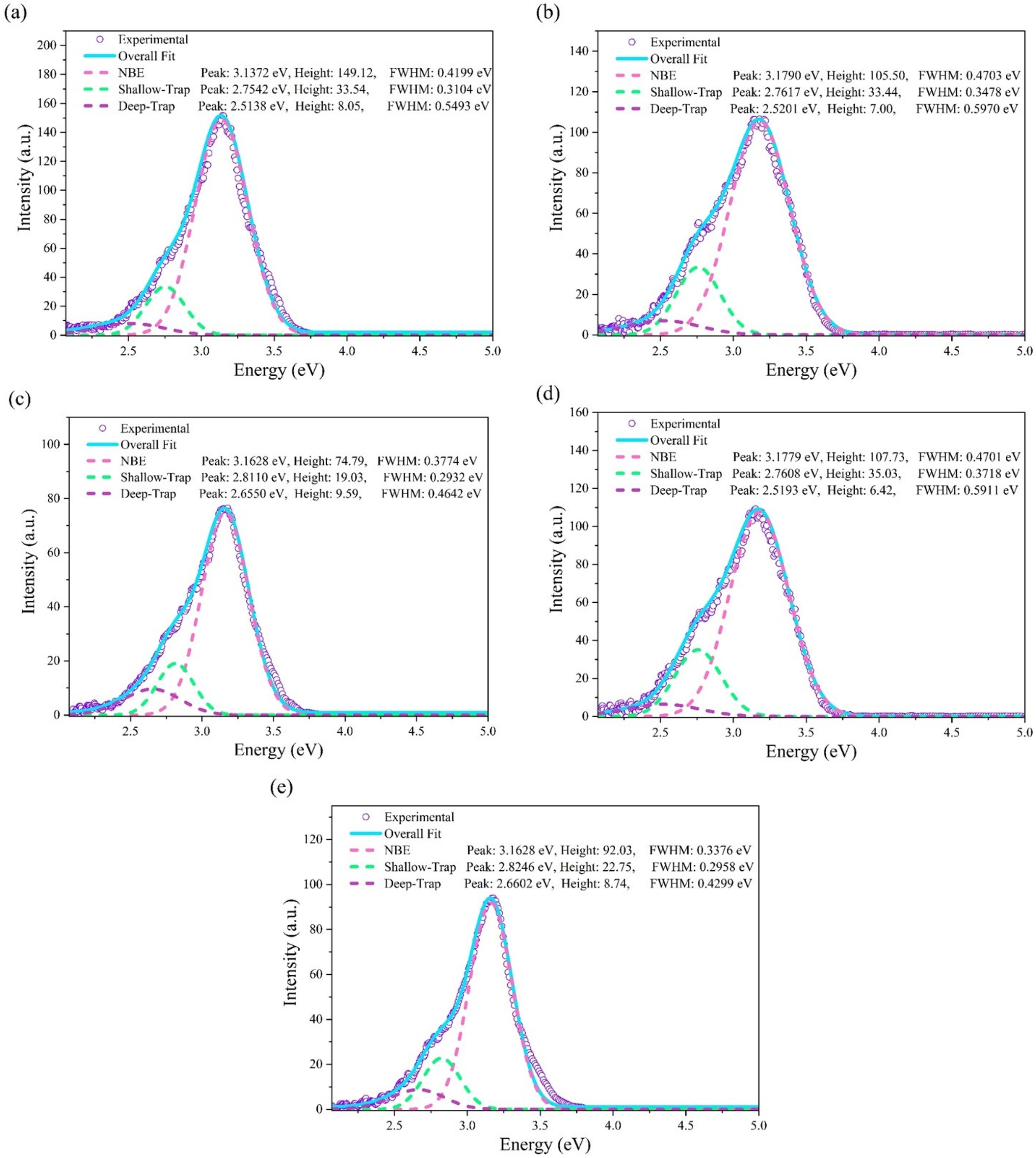

Fig. S7. The deconvolution of the PL spectra for (a) pure, (b) Al-3, (c) Ga-3, (d) Al-5, and (e) Ga-5 samples.

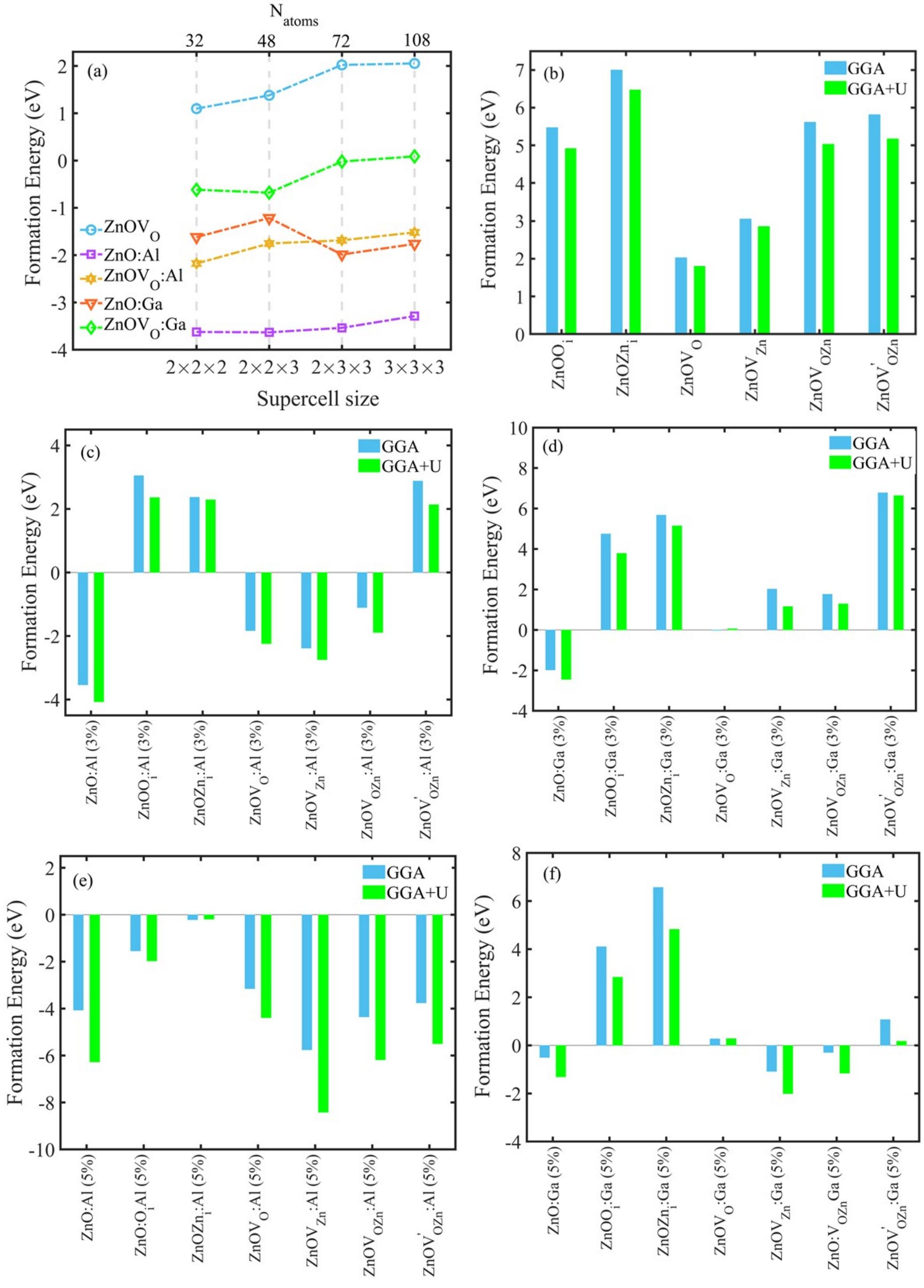

Fig. S8 (a) The formation energy for ZnO:Al and ZnO:Ga states and ZnOVO, ZnOVO:Al and ZnOVO:Ga defects in 2×2×2, 2×2×3, 2×3×3, and 3×3×3 supercells, and (b-f) calculated formation energy by using the GGA and GGA+U approximations under equilibrium conditions for all states and defects of 2×3×3 supercell.

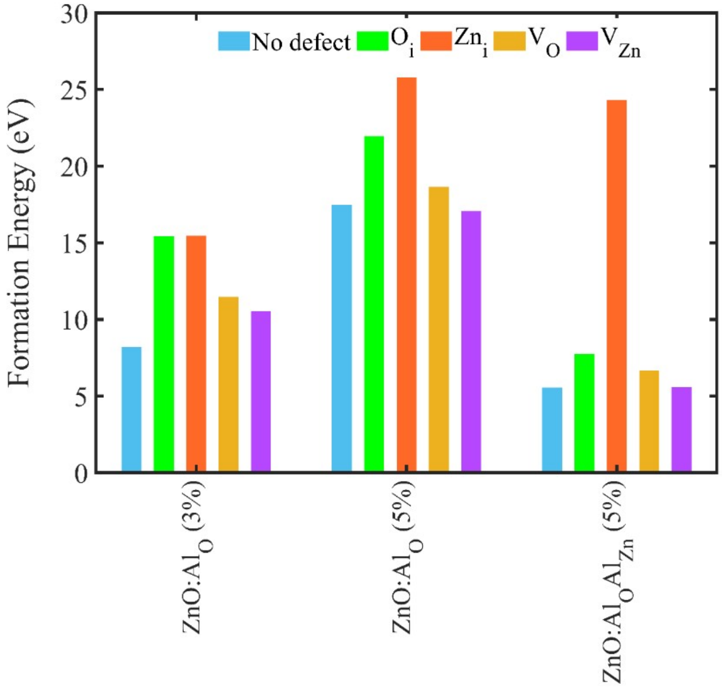

Fig. S9. Intrinsic defect formation energies for 3% and 5% Al-doped ZnO when Al atoms replace O ($ZnO{:}Al_O$ (3%) and $ZnO{:}Al_O$ (5%)) and when Al atoms replace O and Zn atoms. ($ZnO{:}Al_OAl_{Zn}$ (5%)), and under equilibrium conditions.

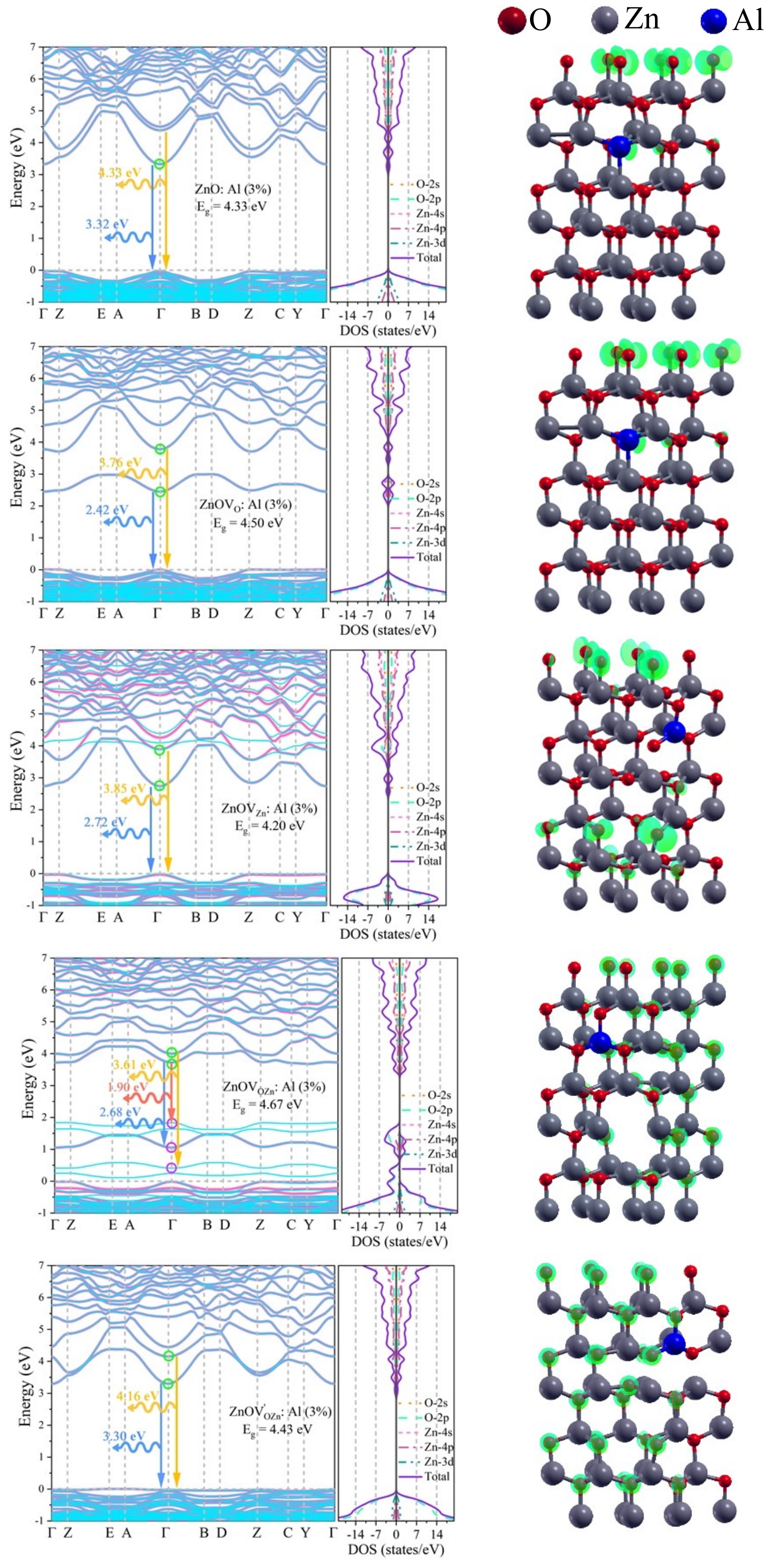

Fig. S10. The spin-polarized band structure, along with total and partial density of states, and spin density distribution (0.0025 a.u.) for 3% Al-doped zinc oxide with oxygen and zinc vacancies. Magenta/cyan bands show spin-up/down states.

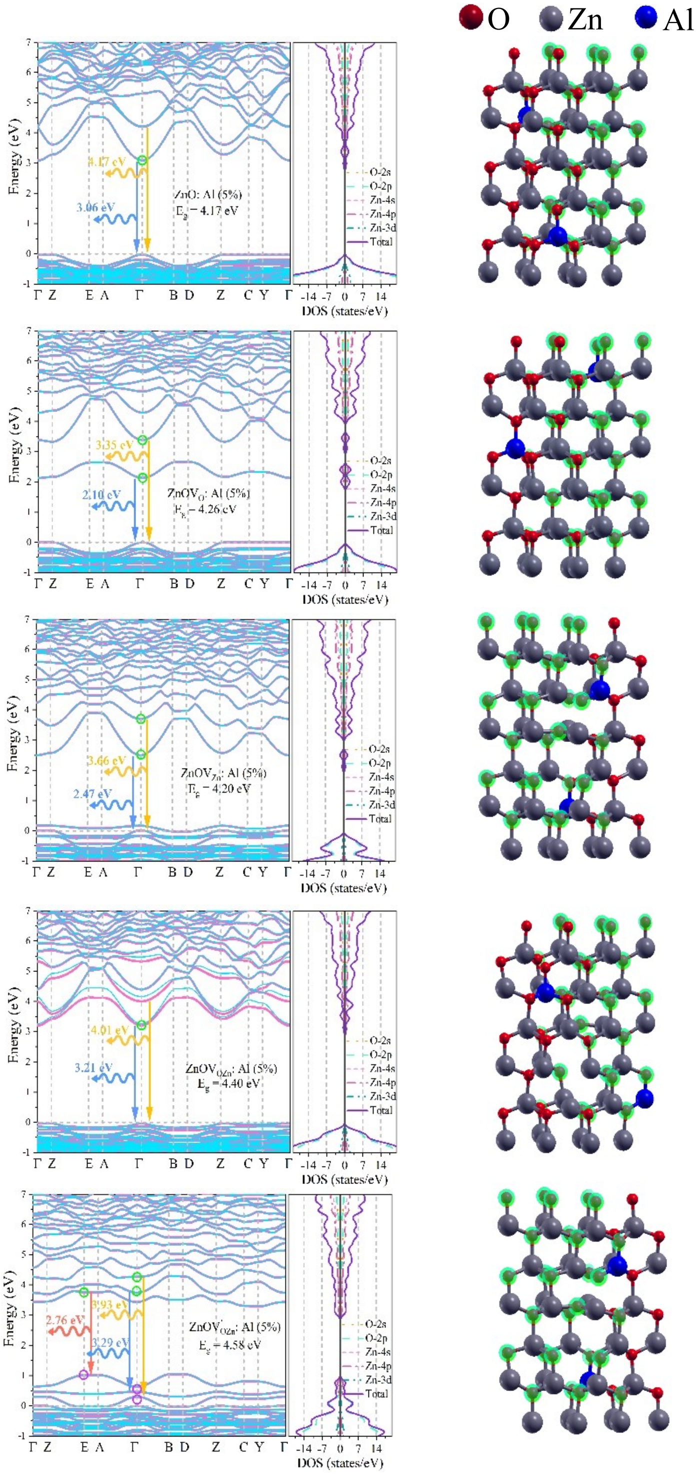

Fig. S11. The spin-polarized band structure, along with total and partial density of states, and electron density distribution (0.25 a.u.) for 5% Al-doped zinc oxide with oxygen and zinc vacancies. Magenta/cyan bands show spin-up/down states.

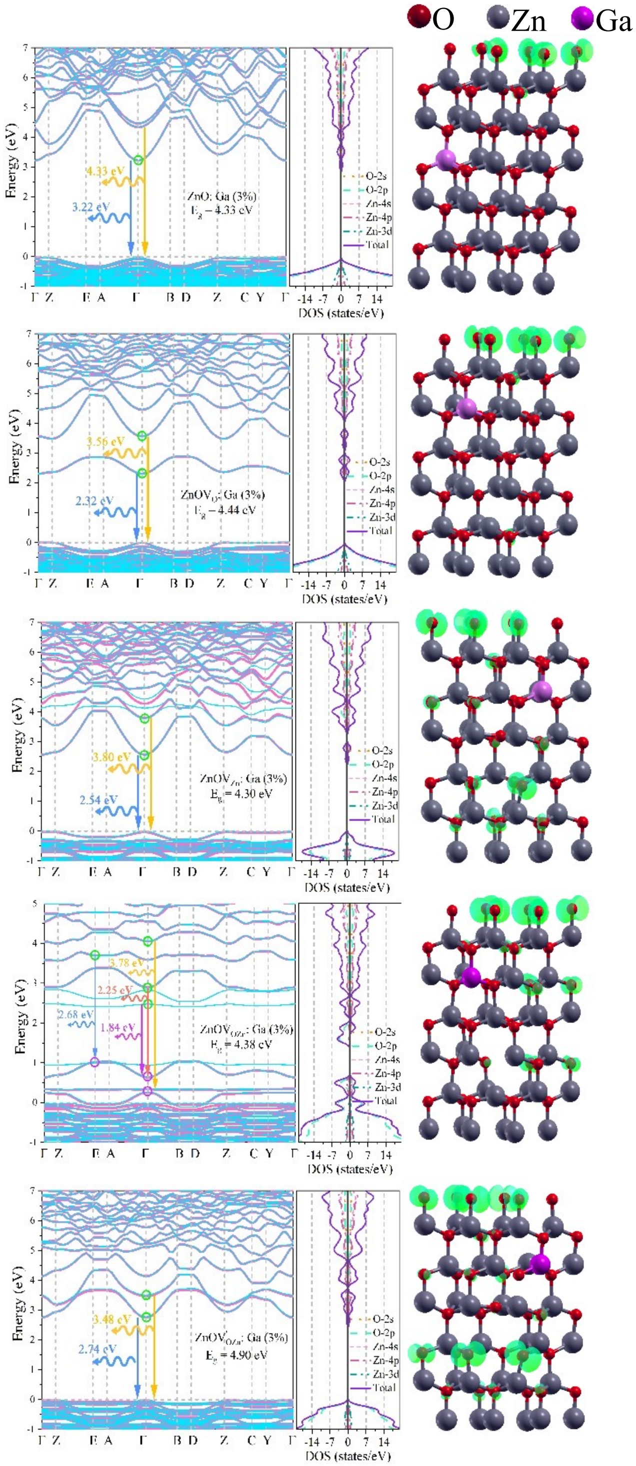

Fig. S12. The spin-polarized band structure, along with total and partial density of states, and spin density distribution (0.0025 a.u.) for 3% Ga-doped zinc oxide with oxygen and zinc vacancies. Magenta/cyan bands show spin-up/down states.

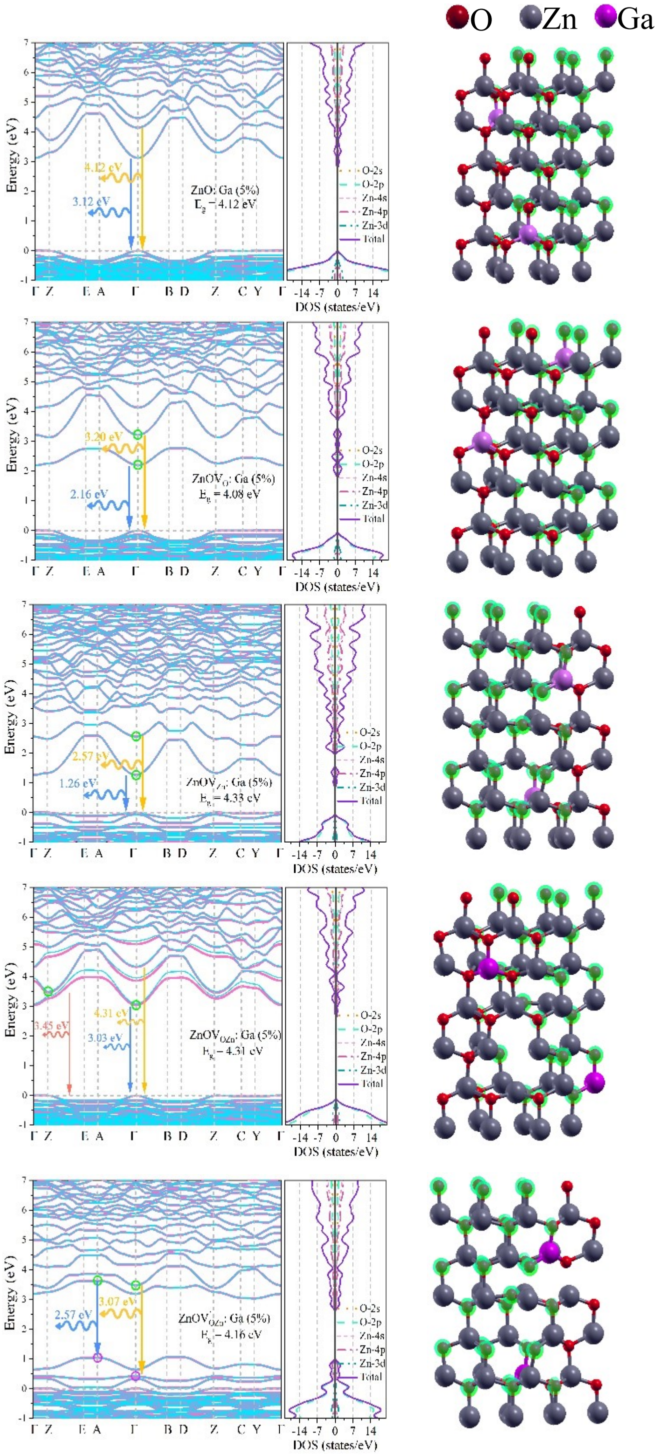

Fig. S13. The spin-polarized band structure, along with total and partial density of states, and electron density distribution (0.25 a.u.) for 5% Ga-doped zinc oxide with oxygen and zinc vacancies. Magenta/cyan bands show spin-up/down states.

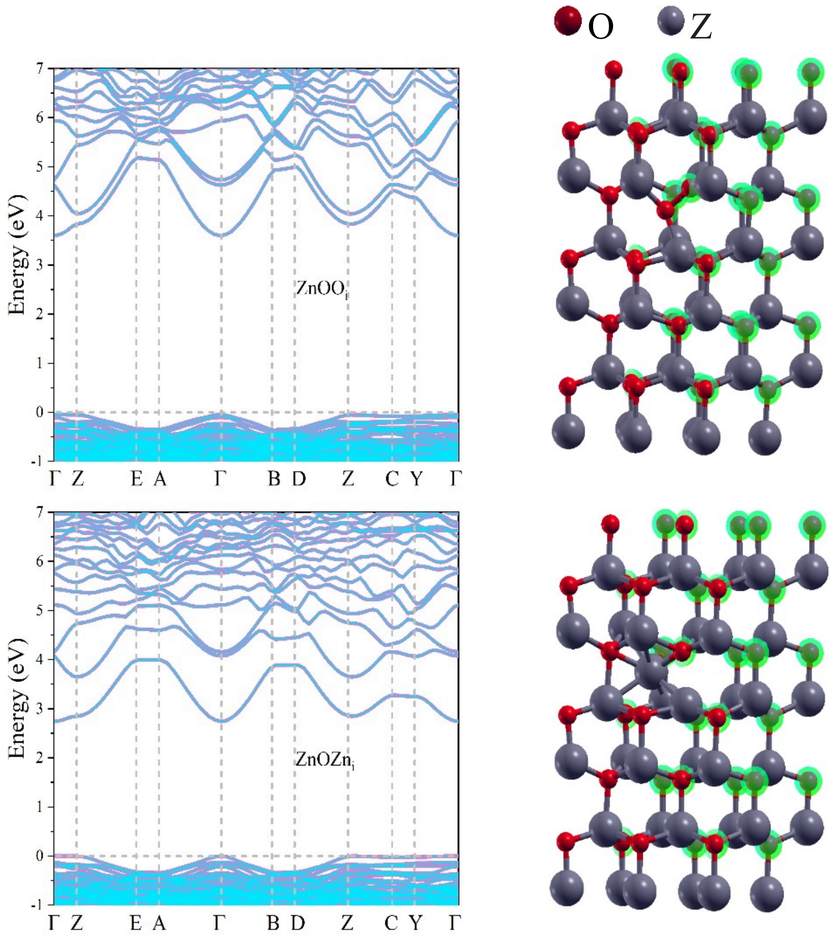

Fig. S14. The spin-polarized band structure, along with total and partial density of states, and electron density distribution (0.25 a.u.) for pure ZnO containing Zn_i and O_i defects. Magenta/cyan bands show spin-up/down states.

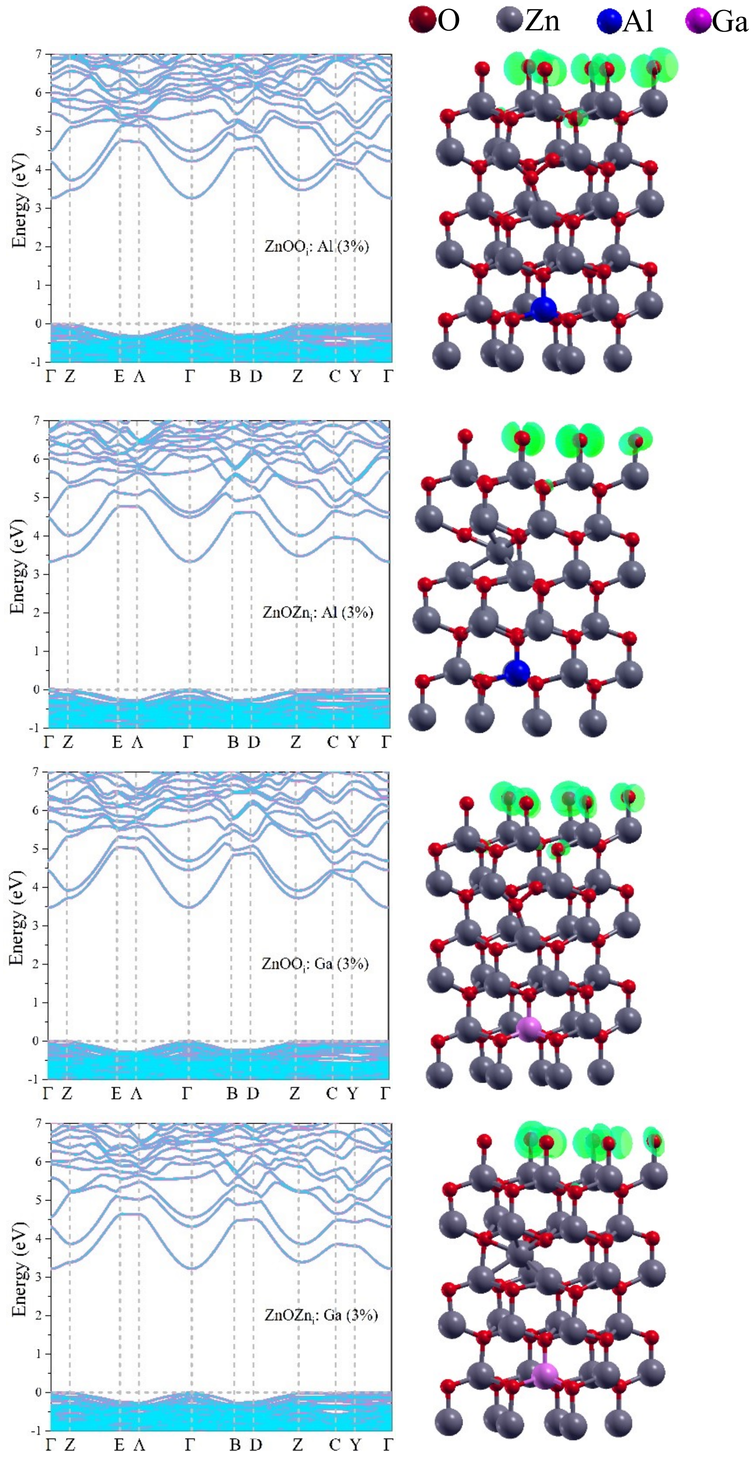

Fig. S15. The spin-polarized band structure, along with total and partial density of states, and spin density distribution (0.0025 a.u.) for 3% Al/Ga-doped ZnO containing Zn$_i$ and O$_i$ defects. Magenta/cyan bands show spin-up/down states.

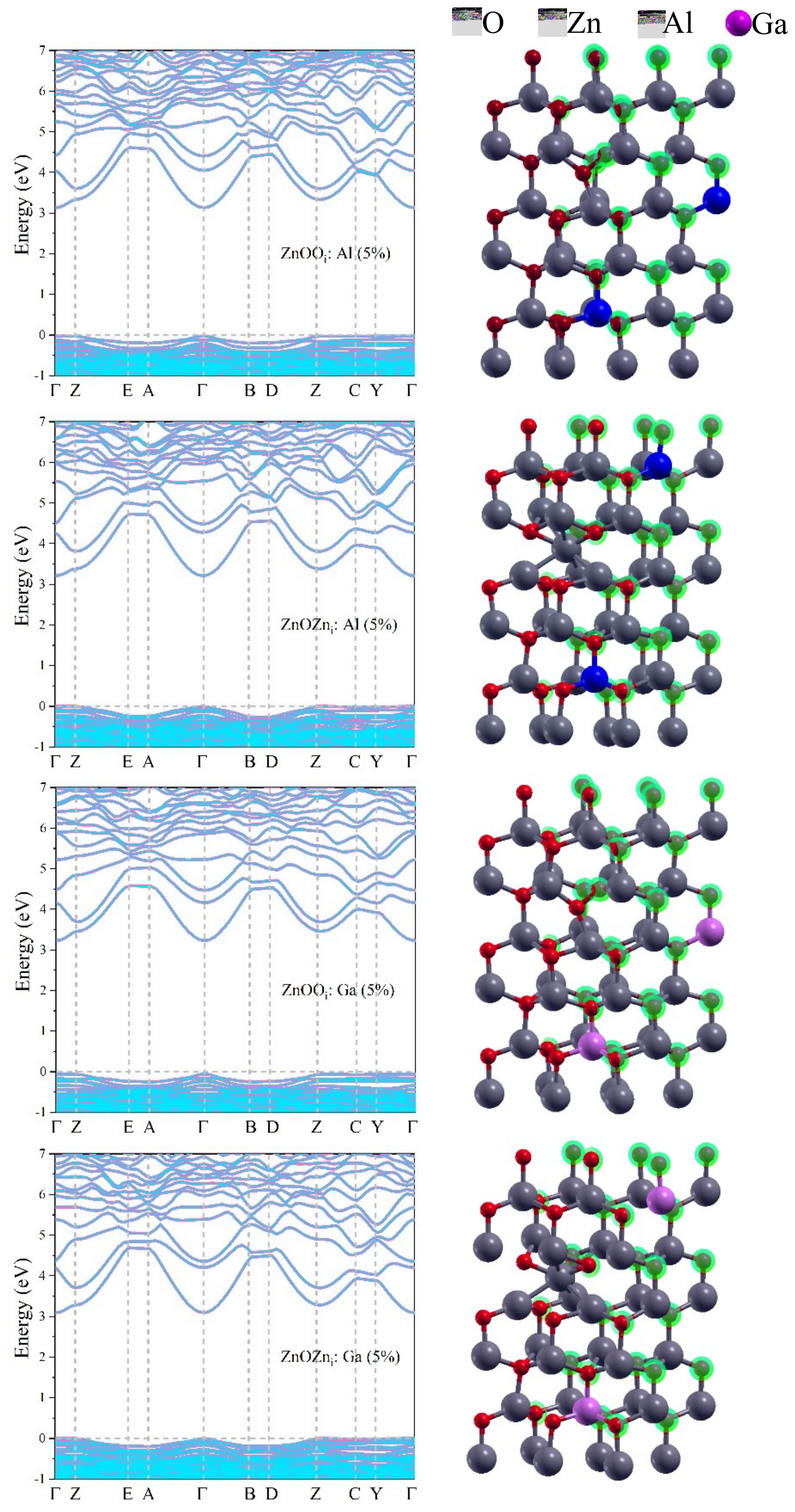

Fig. S16. The spin-polarized band structure, along with total and partial density of states, and electron density distribution (0.25 a.u.) for 5% Al/Ga-doped ZnO containing Zn$_i$ and O$_i$ defects. Magenta/cyan bands show spin-up/down states.

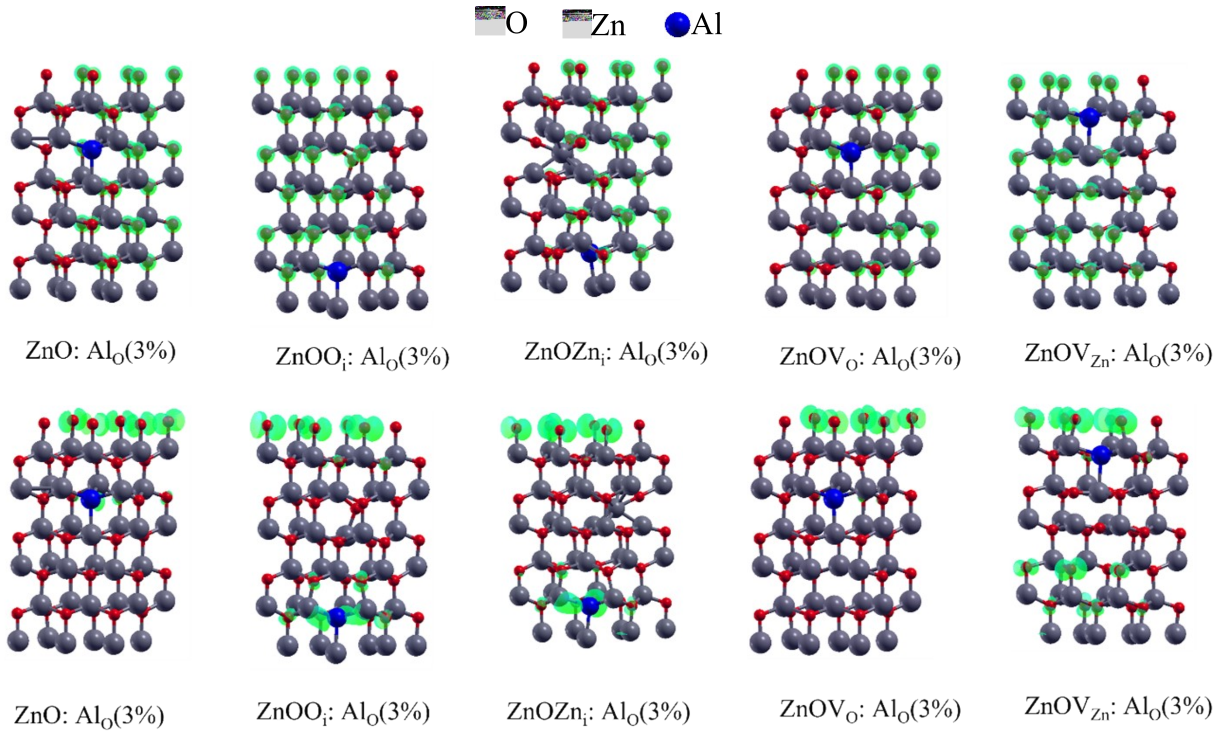

ZnO: $\mathrm{Al_O}$(3%) ZnOO$_i$: $\mathrm{Al_O}$(3%) ZnOZn$_i$: $\mathrm{Al_O}$(3%) ZnOV$_O$: $\mathrm{Al_O}$(3%) ZnOV$_{Zn}$: $\mathrm{Al_O}$(3%)

ZnO: $\mathrm{Al_O}$(3%) ZnOO$_i$: $\mathrm{Al_O}$(3%) ZnOZn$_i$: $\mathrm{Al_O}$(3%) ZnOV$_O$: $\mathrm{Al_O}$(3%) ZnOV$_{Zn}$: $\mathrm{Al_O}$(3%)

Fig. S17. Crystal structure of zinc oxide doped with 3% aluminum when aluminum atoms replace oxygen atoms, with spin density distribution (0.0025 a.u.) (top) and electron density distribution (0.25 a.u.) (bottom).

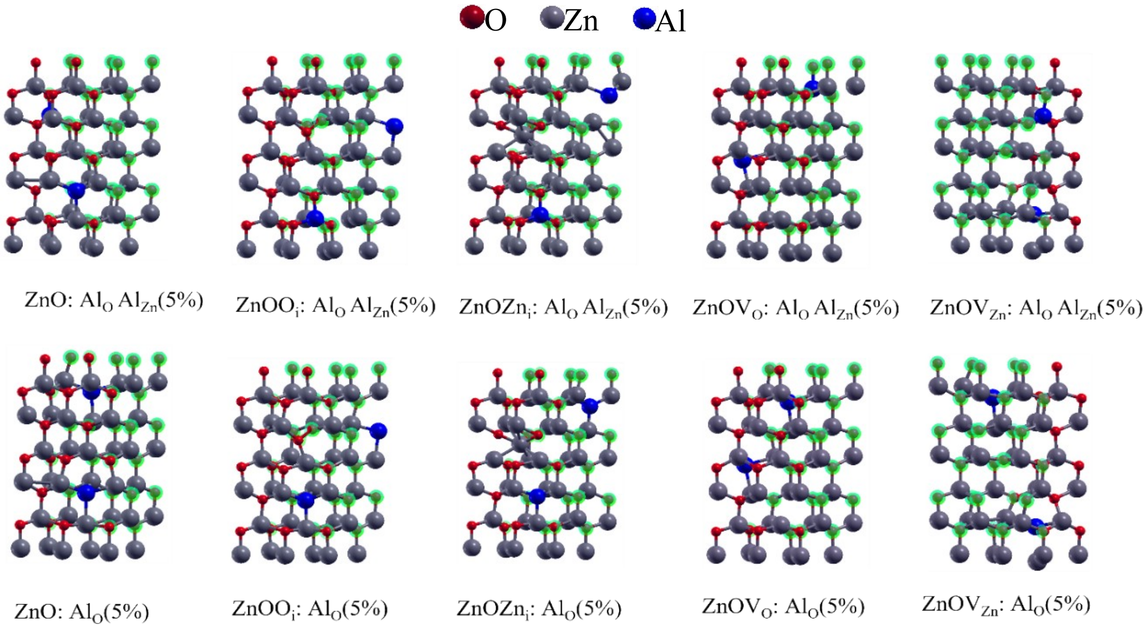

ZnO: $\mathrm{Al_O}$ $\mathrm{Al_{Zn}}$(5%) ZnOO$_i$: $\mathrm{Al_O}$ $\mathrm{Al_{Zn}}$(5%) ZnOZn$_i$: $\mathrm{Al_O}$ $\mathrm{Al_{Zn}}$(5%) ZnOV$_O$: $\mathrm{Al_O}$ $\mathrm{Al_{Zn}}$(5%) ZnOV$_{Zn}$: $\mathrm{Al_O}$ $\mathrm{Al_{Zn}}$(5%)

ZnO: $\mathrm{Al_O}$(5%) ZnOO$_i$: $\mathrm{Al_O}$(5%) ZnOZn$_i$: $\mathrm{Al_O}$(5%) ZnOV$_O$: $\mathrm{Al_O}$(5%) ZnOV$_{Zn}$: $\mathrm{Al_O}$(5%)

Fig. S18. Crystal structure of zinc oxide doped with 5% aluminum when aluminum atoms replace oxygen atoms, with spin density distribution (0.0025 a.u.) (top) and electron density distribution (0.25 a.u.) (bottom).

Table 2. Effective mass ratios of electrons and holes (relative to electron rest mass), electron and hole concentrations (cm^{-3}), and free volume (Å^3) for pure zinc oxide and Al/Ga-doped zinc oxide with dominant defects.

	m_e^*	m_h^*	n	p	V
ZnO	0.4675	0.8532	1.41×10^{-13}	3.43×10^{-13}	-
ZnOV$_{\mathrm{O}}$	0.6735	0.7671	1.82×10^{13}	2.81×10^{-37}	14.00
ZnOV$_{\mathrm{Zn}}$	0.7974	0.9976	1.41×10^{-34}	1.11×10^{-4}	16.83
ZnOV$_{\mathrm{OZn}}$	1.1206	1.1455	3.25×10^{-18}	4.13×10^{-11}	30.82
ZnOV'$_{\mathrm{OZn}}$	1.0266	1.1725	4.39×10^{-26}	0.14	14.11, 17.82
ZnO:Al (3%)	0.8134	0.7018	5.14×10^{12}	8.46×10^{-54}	-
ZnOV$_{\mathrm{O}}$:Al (3%)	0.7641	0.7708	1.84×10^{16}	2.07×10^{-54}	13.81
ZnOV$_{\mathrm{Zn}}$:Al (3%)	0.7435	1.4285	1.66×10^{-28}	8.44×10^{-7}	17.06
ZnOV$_{\mathrm{OZn}}$:Al (3%)	0.7621	2.5078	1.28×10^{-16}	6.38×10^{-47}	31.67
ZnOV'$_{\mathrm{OZn}}$:Al (3%)	4.6630	1.1100	1.25×10^{-39}	2.57×10^{-9}	14.02, 19.34
ZnO:Al (5%)	0.7993	0.8287	8.39×10^{19}	3.167×10^{-58}	-
ZnOV$_{\mathrm{O}}$:Al (5%)	0.7838	0.8286	1.25×10^{25}	1.13×10^{-59}	13.77
ZnOV$_{\mathrm{Zn}}$:Al (5%)	0.8610	2.0004	3.80×10^{-30}	1.56	17.31
ZnOV$_{\mathrm{OZn}}$:Al (5%)	0.7672	1.0017	1.06×10^{-6}	2.12×10^{-53}	30.34
ZnOV'$_{\mathrm{OZn}}$:Al (5%)	1.8159	1.6684	9.34×10^{-21}	1.54×10^{-18}	13.92, 17.82
ZnO:Ga (3%)	0.7404	0.7156	6.22×10^{9}	1.92×10^{-52}	-
ZnOV$_{\mathrm{O}}$:Ga (3%)	0.7369	0.7127	9.98×10^{14}	1.84×10^{-53}	13.98
ZnOV$_{\mathrm{Zn}}$:Ga (3%)	0.7498	1.4309	3.03×10^{-31}	1.03×10^{-3}	17.28
ZnOV$_{\mathrm{OZn}}$:Ga (3%)	5.1003	0.7647	4.91×10^{-14}	1.26×10^{-38}	29.16
ZnOV'$_{\mathrm{OZn}}$:Ga (3%)	0.9860	1.2147	1.04×10^{-6}	2.44×10^{-19}	14.12, 17.84
ZnO:Ga (5%)	0.7364	0.8332	4.77×10^{16}	7.43×10^{-54}	-
ZnOV$_{\mathrm{O}}$:Ga (5%)	0.6902	0.7666	1.72×10^{8}	2.09×10^{-53}	13.80
ZnOV$_{\mathrm{Zn}}$:Ga (5%)	0.7498	1.4309	1.42×10^{-30}	1.61×10^{8}	17.36
ZnOV$_{\mathrm{OZn}}$:Ga (5%)	0.7911	0.8314	1.05×10^{-9}	2.59×10^{-48}	19.16
ZnOV'$_{\mathrm{OZn}}$:Ga (5%)	0.9860	1.2147	1.25×10^{-16}	1.05×10^{-15}	14.00, 18.73

References for Supporting Information

1. Saidani, A. *et al.* Effect of calcination temperature on the photocatalytic activity of precipitated ZnO nanoparticles for the degradation of rhodamine B under different light sources. *Water* **17**, 32 (2024).

2. Neese, F., Harris, R. K. & Wasylishen, R. L. Quantum chemistry and EPR parameters. (2017).

3. Giovannini, T., Lafiosca, P., Chandramouli, B., Barone, V. & Cappelli, C. Effective yet reliable computation of hyperfine coupling constants in solution by a QM/MM approach: Interplay between electrostatics and non-electrostatic effects. *J. Chem. Phys.* **150**, (2019).

4. Green, M. A. Intrinsic concentration, effective densities of states, and effective mass in silicon. *J. Appl. Phys.* **67**, 2944–2954 (1990).

5. Spustaka, A., Millers, D., Einbergs, E., Vitola, V. & Vanags, E. Luminescence of ZnO: Ga ceramics under sub-threshold electron irradiation. *Opt. Mater. (Amst).* **126**, 112181 (2022).

6. Chen, L. *et al.* Comparative study on fluorescence decay time of doped ZnO crystals under \$α\$ and \$β\$ excitation. *Nucl. Instruments Methods Phys. Res. Sect. A Accel. Spectrometers, Detect. Assoc. Equip.* **933**, 71–74 (2019).

7. Sturge, M. D. Electrons and Holes in Semiconductors. *Stat. Therm. Phys.* 269–290 (2020) doi:10.1201/9781315275529-19.

8. Experimental and DFT investigation of electronic structure, defect states, and visible luminescence in Co-doped ZnO nanocrystals. *J. Appl. Phys.* **138**, 145102 (2025).

9. Kumar, P. *et al.* Recent advancements in pure and doped zinc oxide nanostructures for UV photodetectors application. *Phys. B Condens. Matter* **707**, 417177 (2025).

10. Vidya, R. *et al.* Energetics of intrinsic defects and their complexes in ZnO investigated by density functional calculations. *Phys. Rev. B* **83**, 45206 (2011).

11. Wang, Z. *et al.* Vacancy cluster in ZnO films grown by pulsed laser deposition. *Sci. Rep.* **9**, 1–10 (2019).

12. Fabbri, F. *et al.* Zn vacancy induced green luminescence on non-polar surfaces in ZnO nanostructures. *Sci. Rep.* **4**, 1–6 (2014).

13. Lyons, J. L., Janotti, A. & de Walle, C. G. Role of Si and Ge as impurities in ZnO. *Phys. Rev. B* **80**, 205113 (2009).

14. Aleinawi, M. H. *et al.* Spectroscopic probing of Mn-doped ZnO nanowires synthesized via a microwave-assisted route. *J. Phys. Chem. C* **126**, 4229–4240 (2022).

15. Ahn, C. H., Kim, Y. Y., Kim, D. C., Mohanta, S. K. & Cho, H. K. A comparative analysis of deep level emission in ZnO layers deposited by various methods. *J. Appl. Phys.* **105**, (2009).

16. Cabral, L. *et al.* Insights into the nature of optically active defects of ZnO. *J. Lumin.* **227**, 117536 (2020).